In Vivo Molecular Imaging of Breast Cancer Metabolic Heterogeneity Using [1-^{13}C]Pyruvate-d$_3$ Hyperpolarized By Reversible Exchange With Parahydrogen

*Stefan Petersen,‡ Luca Nagel, ‡ Philipp R. Groß, Henri de Maissin, Robert Willing, Lisa Heß, Julia Mitschke, Nicole Klemm, Judith Treiber, Christoph A. Müller, Stephan Knecht, Ilai Schwartz, Moritz Weigt, Michael Bock, Dominik von Elverfeldt, Maxim Zaitsev, Eduard Y. Chekmenev, Jan-Bernd Hövener, André F. Martins, Franz Schilling, Thomas Reinheckel, Andreas B. Schmidt**

‡ shared first authorship

* correspondence: andreas.schmidt@uniklinik-freiburg.de

S. Petersen, P. R. Groß, H. de Maissin, R. Willing, C. A. Müller, M. Weigt, M. Bock, D. von Elverfeldt, M. Zaitsev, A. B. Schmidt
Division of Medical Physics, Department of Radiology, University Medical Center Freiburg, Faculty of Medicine, University of Freiburg, Killianstr. 5a, Freiburg 79106, Germany

P. R. Groß, H. de Maissin, R. Willing, L. Heß, M. Bock, D. von Elverfeldt, M. Zaitsev, T. Reinheckel, A. B. Schmidt
German Cancer Consortium (DKTK), partner site Freiburg and German Cancer Research Center (DKFZ), Im Neuenheimer Feld 280, Heidelberg 69120, Germany

L. Nagel, F. Schilling
Department of Nuclear Medicine, TUM School of Medicine and Health, Klinikum rechts der Isar, Technical University of Munich, Munich, Germany, Ismaninger Str. 22, Munich, 81675, Germany

L. Heß, J. Mitschke, J. Treiber, N. Klemm, T. Reinheckel
Institute of Molecular Medicine and Cell Research, Faculty of Medicine, University of Freiburg, Stefan-Meier-Str. 17, Freiburg 79104, Germany

C. A. Müller, S. Knecht, I. Schwartz
NVision Imaging Technologies GmbH, Wolfgang-Paul-Str. 2, 89081 Ulm, Germany

E. Y. Chekmenev, A. B. Schmidt
Department of Chemistry, Integrative Biosciences (Ibio), Karmanos Cancer Institute (KCI), Wayne State University, Detroit, Michigan 48202, United States

J.-B. Hövener
Section Biomedical Imaging, Molecular Imaging North Competence Center MOINCC, Department of Radiology and Neuroradiology, University Hospital Schleswig Holstein, Kiel University

A. F. Martins
Werner Siemens Imaging Center, Department of Preclinical Imaging and Radiopharmacy, Eberhard Karls University Tübingen, Röntgenweg 13, 72076 Tubingen, Germany

A. F. Martins
Cluster of Excellence iFIT (EXC 2180) "Image-Guided and Functionally Instructed Tumor Therapies", Eberhard Karls University Tübingen

A. F. Martins
German Cancer Consortium (DKTK), partner site Tubingen and German Cancer Research Center (DKFZ), Im Neuenheimer Feld 280, Heidelberg 69120, Germany

F. Schilling
Munich Institute of Biomedical Engineering, Technical University of Munich, Garching, Germany, Boltzmannstr. 11, Garching 85748, Germany

F. Schilling
German Cancer Consortium (DKTK), partner site Munich and German Cancer Research Center (DKFZ), Im Neuenheimer Feld 280, Heidelberg 69120, Germany

Abstract

Metabolic MRI using hyperpolarized (HP) [1-^{13}C]pyruvate is promising for diagnostic medicine, allowing the study of cancer metabolism and early detection of therapy response. However, a possible widespread and routine use requires high-throughput and user-friendly technologies to produce the hyperpolarized media. Recently, we introduced a fast (6 min) and cost-effective method using Spin-Lock Induced Crossing and Signal Amplification By Reversible Exchange (SLIC-SABRE) at μT fields and a rapid purification to produce biocompatible HP solutions of aqueous pyruvate. In this study, we used SLIC-SABRE to conduct *in vivo* tumor metabolic imaging in a transgenic breast cancer mouse model (MMTV-PyMT). In agreement with previous HP MRI cancer studies, an elevated lactate metabolism was found in tumors compared to healthy breast tissue, heart, and vasculature, as well as distinct metabolic profiles within different tumor compartments. These findings suggest a potential link between lactate-to-pyruvate ratios and the varying levels of tumor cell proliferation and apoptosis observed by histological analyses. Our results underscore the potential of SABRE to enhance the accessibility and throughput of HP MRI, thereby advancing cancer research and diagnostic oncology.

1. Introduction

Cancer remains a significant challenge in modern medicine, with breast cancer representing one of the most prevalent and heterogeneous malignancies.[1] Despite incremental advancements in therapies, including surgery, radiation, and targeted therapies, there remains an urgent medical need to improve clinical outcomes. The complexity of cancer, underscored by its molecular diversity and intratumoral heterogeneity, necessitates personalized approaches for accurate diagnosis and effective treatment guided by non-invasive *in vivo* imaging.[2]

Imaging technologies are playing a pivotal role in cancer care by providing non-invasive assessments of tumor characteristics and treatment responses. Traditional anatomical imaging techniques often cannot provide molecular-level information of cancer development. To address this limitation, molecular imaging techniques have emerged with breakthrough applications.[3,4]

Hyperpolarized magnetic resonance imaging (HP MRI), allows for transient signal enhancements of over 10,000-fold.[5] HP MRI offers non-invasive insights into biochemical pathways *in vivo*, without ionizing radiation. HP MRI is the only technology that enables the visualization of metabolic conversion *in vivo* with spatial and real-time temporal resolution. HP [1-^{13}C]-pyruvate showed great promise for investigating cancer as it is a central metabolite in

energy metabolic pathways at the intersection of glycolysis and the TCA cycle. Pyruvate has been used to image metabolism in many cancers, including prostate cancer,[6] glioblastoma,[7] and bone and liver metastases,[8] providing unprecedented insights into tumor biology. Clinically, detecting the Warburg effect - enhanced glycolysis and lactate formation even in the presence of high oxygen levels in tumors - provides essential information regarding tumor grading[9] and active surveillance of therapy response in oncological patients.[10–12] HP [1-^{13}C]-pyruvate MRI is under investigation in over 50 clinical trials.[4]

The implementation of HP ^{13}C MRI is currently impeded by several challenges, hindering its widespread application and clinical translation. Notably, these include the short lifetime of the hyperpolarized agent, high cost, large size of the equipment, low throughput, and the requirement for highly trained personnel, all of which contribute to its slow development.

Dissolution Dynamic Nuclear Polarization (dDNP) is the leading technology for producing HP [1-^{13}C]-pyruvate.[13] It requires strong magnetic fields (typically 5-7 T), cryogenic temperatures (<2K), and microwave irradiation to polarize agents in the solid phase, followed by rapid thawing and dissolution with superheated water to transfer HP metabolites into the liquid phase. Preparing HP boluses is elaborate and time-consuming, taking about an hour for a bolus of HP [1-^{13}C]pyruvate; however, many molecular probes can be polarized with dDNP.[12,14] Impressive results of HP MRI have driven ongoing efforts to improve dDNP[15–18] and develop alternative technologies for faster, more versatile, and cost-effective HP media production.[19,20] Parahydrogen-induced polarization (PHIP)[21,22] technologies offer a solution to several challenges by providing rapid hyperpolarization with simple, low-footprint hardware and reduced production costs.[19] PHIP involves the permanent addition of parahydrogen to the substrate through direct or side-arm hydrogenation (PHIP-SAH).[23] This method, particularly with HP [1-^{13}C]pyruvate, has been used in *in vivo* cardiac[24] and tumor studies[25–27] in mice and is being developed for commercial preclinical and clinical devices. However, identifying and synthesizing suitable unsaturated precursors is often challenging and costly. Additionally, the chemical modification (i.e., hydrogenation) done seconds before the *in vivo* administration introduces regulatory complexities and may require manufacturing licenses for clinical applicants in some countries.[19]

A non-hydrogenative PHIP referred to as SABRE (Signal Amplification By Reversible Exchange) has been presented by Duckett and coworkers.[20,28,29] SABRE employs a reversible exchange of parahydrogen and suitable substrates with an iridium catalyst[30], allowing for continuous polarization transfer without altering the chemical structure of the substrate.[31,32] Therefore, the method combines the advantages of PHIP - such as speed, low cost, and

simplicity - with some of the flexibility of dDNP, which has enabled the ^{13}C and ^{15}N SABRE hyperpolarization of multiple agents[20,33–35], including [1-^{13}C]-pyruvate[29,36–39]. Consequently, the translation of SABRE to preclinical studies and clinical settings is highly promising.

Recently, we introduced a fast and cost-effective method using SABRE and Spin-Lock Induced Crossing (SLIC-SABRE)[40,41] at microtesla fields,[42,43] which can polarize [1-^{13}C]pyruvate-d_3 to over 20%, sufficient for ^{13}C MRI. Initially, this was achieved in a toxic methanol solution containing the iridium-based exchange catalyst. However, a rapid purification process has enabled us to produce HP solutions of aqueous pyruvate suitable for *in vivo* applications, **Figure 1**.[44] The deuteration of pyruvate results in an increased polarization lifetime without affecting the kinetics of pyruvate metabolism.[42,45]

In the present study, we demonstrate ^{13}C MRI of cancer using aqueous [1-^{13}C]pyruvate-d_3 hyperpolarized using SLIC-SABRE. Focusing on transgenic breast cancer mice, we reveal considerable lactate production and pronounced intra- and intertumoral heterogeneity of the lactate metabolism, which correlates well with histological results.

2. Results and Discussion

2.1. SABRE-Hyperpolarized [1-^{13}C]-Pyruvate-d_3

50 mM [1-^{13}C]-pyruvate-d_3 were hyperpolarized to up to 24% in 600 µL methanol-d_4 using SLIC-SABRE at a 50 µT static magnetic field. Subsequently, 600 µL phosphate-buffered solution (PBS) of D_2O were added and the sample was evacuated to evaporate methanol-d_4 at approximately 100 mT, 5 mbar, and 100 °C (250 µM residual methanol). The aqueous solution was then filtered to remove the precipitated iridium catalyst, resulting in [1-^{13}C]-pyruvate-d_3 in D_2O solution of pH 6.5 – 7, ready for administration to the mice, **Figure 1**. This way, we efficiently produced a batch of 30-mM aqueous, pH neutral HP [1-^{13}C]-pyruvate-d_3, hyperpolarized up to $P_{13C} \approx 10$ % in less than 6 minutes, **Figure S1**. Further experimental details are provided in the SI.

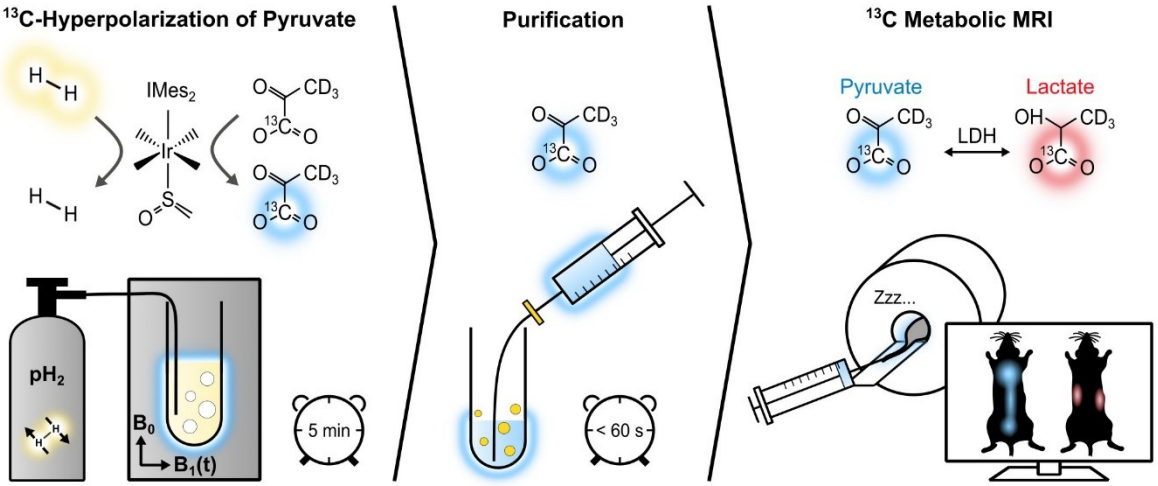

Figure 1. The experimental protocol for *in vivo* metabolic MRI. Initially, [1-^{13}C]-pyruvate-d_3 undergoes hyperpolarization via reversible exchange with parahydrogen at an iridium complex. Parahydrogen is bubbled through an NMR tube containing the SABRE reaction solution while applying a 2 μT SLIC radiofrequency field in a 50 μT static magnetic field (**left**). Subsequently, the hyperpolarized [1-^{13}C]-pyruvate-d_3 is transferred from methanol-d_4 to a PBS of D_2O, and the resulting solution is collected in a syringe after filtration to remove the non-water-soluble iridium complex (**center**). This biocompatible [1-^{13}C]-pyruvate-d_3 solution is then administered to the tumor-bearing mice, allowing for the monitoring of its conversion into downstream metabolic products, i.e., [1-^{13}C]-lactate-d_3 (**right**).

2.2. Tumor Metabolic Imaging

To investigate the efficacy of SABRE hyperpolarized pyruvate in assessing tumor-specific metabolic processes *in vivo*, a transgenic breast cancer model (mouse mammary tumor virus – polyoma virus middle tumor-antigen; MMTV-PyMT) was employed.[46–48] This viral oncogene activates various oncogenic signals in the mammary epithelium. Most notably, it hyper-activates the phosphoinositide 3-kinase (PI3K) pathway, mimicking a common characteristic observed in approximately 70% of breast cancer patients. The onset of mammary adenomas in MMTV-PyMT mice typically occurs at about 6 weeks of age, rapidly progressing to large, invasive, and poorly differentiated carcinomas within 8 weeks. The numbering of breast tumors and mammary glands is shown in **Figure S2**.

Vital parameters of the rodents were continuously monitored throughout the MRI procedure (see Supporting Information (SI) for details and ethics).

For MRI, a dedicated mouse ^{1}H/^{13}C quadrature resonator (inner diameter of 3.5 cm, V-XQ-HQ-070-02222, Rapid Biomedical GmbH, Germany) and a 7 T preclinical MRI system (Biospec 70/20, PV6.0.1, Bruker, Germany) were utilized. Following the injection of a single bolus of a

30mM HP [1-^{13}C]-pyruvate-d_3 solution through the tail vein (≤5 µL/g mouse weight), ^{13}C images were acquired using center-out phase encoded free-induction decay chemical shift imaging (FID-CSI) to monitor pyruvate-to-lactate conversion. The FID-CSI sequence was chosen for its known robustness. A cohort of six MMTV-PyMT mice (age: 10-14 weeks, weight: approximately 24g) exhibiting various tumor stages were investigated.

Metabolic imaging revealed prominent lactate metabolism within tumor regions, showcasing the heterogeneous nature of the cancers both anatomically and metabolically. Metabolic imaging results from three of these mice are presented in subsequent sections, while the remaining investigations, along with metabolite signal evolution from all experiments, are provided in the Supplementary Information.

2.2.1. Mouse A – Localized Metabolic Imaging

Mouse A (age: 13 weeks, weigh 24 g) with localized nodules characterized by palpable tumors in all 10 mammary glands. For MRI analysis, an axial region of interest (ROI) is selected that included mammary glands 1, 2, and 7, the lungs, the lower heart ventricles, and the forelimbs, **Figure 2**.

Anatomical ^{1}H MRI revealed the distinct tumorous nodes with varying sizes surrounding the forelimbs. The largest observed diameter of a single mammary carcinoma was ≈ 13 mm at gland 1. Most tumor areas exhibited similar T_2w intensity despite differences in node size, **Figure 2**. Intense lactate signals were observed in the tumors. Although the native ^{13}C MRI resolution is limited, the muscle, particularly the front legs, were still distinguishable from the surrounding tumor tissue in the ^{13}C-lactate images, **Figure 2**. Large pyruvate and lactate signals were also observed in the heart, but the lactate-to-pyruvate ratio is negligible compared to the other regions. Analysis of the signal-time curves detected the arrival of the pyruvate bolus and subsequent formation of downstream lactate in the tumor and, to a lesser extent, in the heart, **Figure S3**. Interestingly, comparing the tumors, the tumor on gland 1 seems to have higher lactate and lactate-to-pyruvate levels than the tumors on gland 2 and 7. Indeed, corresponding histology with Ki67 staining indicated higher cell proliferation levels in tumor 1.

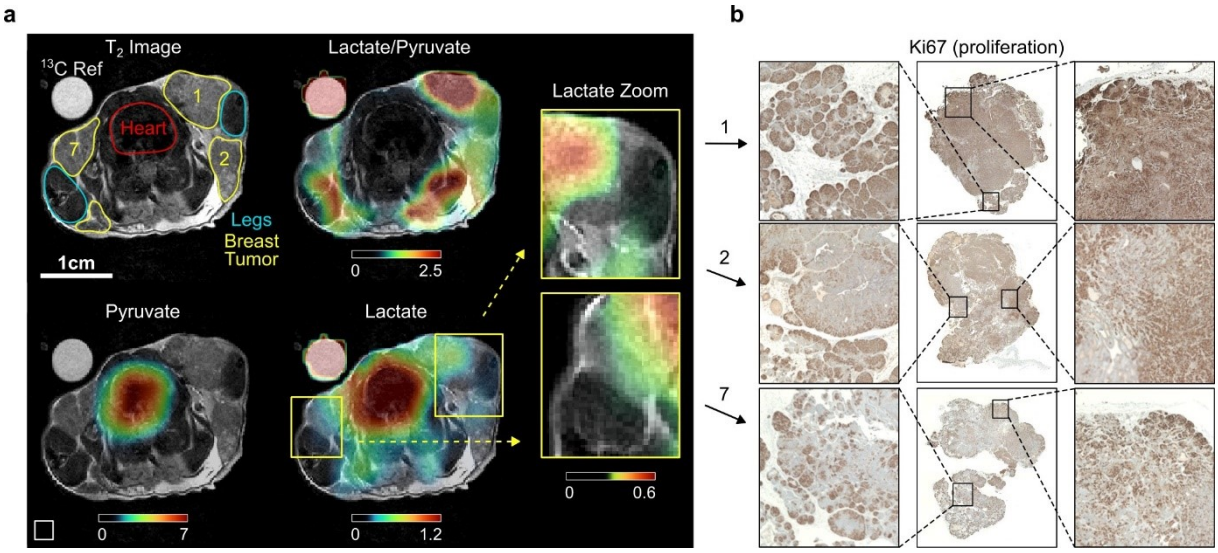

Figure 2. *In vivo* ^{1}H T_2w MRI and dynamic ^{13}C chemical shift imaging of PyMT mouse A after administering SABRE-hyperpolarized [1-^{13}C]-pyruvate-d_3, and histology (Ki67 staining) of the imaged tumors. **a**, Axial anatomic ^{1}H MRI showing the tumors on mammary gland 1, 2 and 7, heart, legs, and a ^{13}C-lactate reference (left). The anatomic slice is superimposed with time-summated and interpolated ^{13}C-lactate/^{13}C-pyruvate (top right), ^{13}C-pyruvate (bottom left) and ^{13}C-lactate signal (bottom right). The lactate signal is enhanced in the breast tumors compared to other non-cancerous tissue (e.g., leg muscle). Note that low lactate signals can lead to high lactate-to-pyruvate ratios without significance if the pyruvate signal in the same voxel is negligible (no thresholding was applied to the ratio maps). The white box (bottom left) indicates the native CSI-FID resolution. **b**, Histology of all three breast tumors with Ki67 staining indicates cell proliferation (brown). Remarkably, the tumor on mammary gland 1 has a significantly higher lactate-to-pyruvate ratio and appears to be more proliferative than other tumors.

2.2.2. Mouse B – Imaging tumor heterogeneity

Mouse B (age: 12 weeks, weigh 24 g) presented with advanced breast cancer characterized by palpable smaller tumors in mammary glands 4 and 9, and larger nodes in glands 2 and 3. No tumor was palpable in the contralateral mammary gland 7. Hence, a cross section of the upper chest covering mammary glands 2, 3, and 7 was subjected to MRI analysis to examine differences in tumorous and healthy-appearing breast tissue, **Figure 3**.

Anatomical ^{1}H MRI revealed the tumorous nodes 2 and 3, with approximate maximum diameters of ≈10-12 mm, respectively. Interestingly, while 2 and 3 were similar in size, 3 exhibited a conspicuous tumor area with enhanced intensity in the T_2-weighted MRI images

(hyper-intense, T_2w+). Anatomical MRI revealed no apparent abnormalities in gland 7, which additionally appeared significantly smaller compared to 2 and 3, **Figure 3**.

The HP ^{13}C MRI data showed the strongest ^{13}C pyruvate and lactate signals in the heart. The lactate level was elevated in the tumor compared to the contralateral non-cancerous appearing breast tissue (gland 7). The T_2w+ region exhibited lower pyruvate and lactate signals than the hypo-intense (T_2w-) region, suggesting lower metabolic activity and perfusion, **Figure 3**. Histological examination of the tumors revealed the onset of apoptosis in the T_2w+ region but higher proliferation in the T_2w- region, **Figure 3b**.

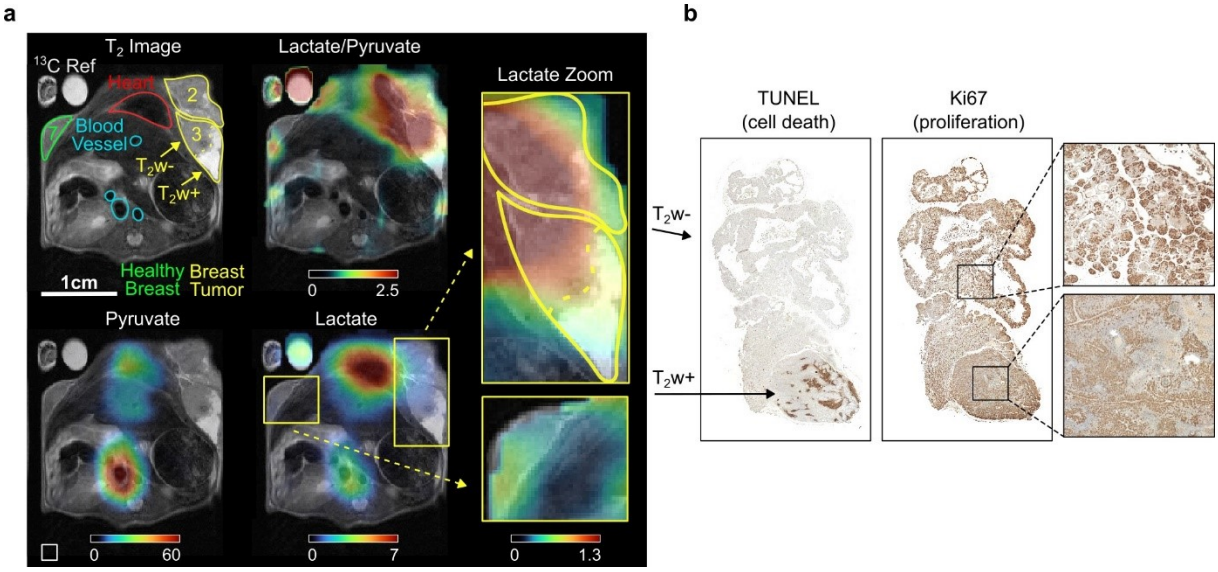

Figure 3. *In vivo* ^{1}H T_2w MRI and ^{13}C chemical shift imaging of PyMT mouse B after administering SABRE-hyperpolarized [1-^{13}C]-pyruvate-d_3 and histology (Ki67 staining) of the imaged tumors. **a**, Axial anatomic ^{1}H MRI showing the tumors on mammary gland 2 and 3, non-cancerous appearing breast tissue on gland 7, heart, blood vessels, and a ^{13}C-lactate reference (left). The anatomic slice is superimposed with the interpolated ^{13}C-lactate/^{13}C-pyruvate (top right), ^{13}C-pyruvate (bottom left) and ^{13}C-lactate signal (bottom right). The lactate signal is enhanced in the breast tumors (2 and 3) compared to the non-cancerous appearing breast tissue on mammary gland 7. The heterogeneous breast tumor on mammary gland 3 divides into a hyper-intense (T_2w+) region with lower lactate and lactate-to-pyruvate signals and a hypo-intense (T_2w-) tumor region with higher signals. The white box indicates the native CSI-FID resolution. **b**, Histology of the breast tumor with TUNEL staining indicating ongoing apoptosis in the T_2w+ region (left) and Ki67 staining indicating cell proliferation in the T_2w- region (right).

2.2.3. Mouse C - Imaging tumor heterogeneity

Mouse C (age: 13 weeks, weigh 26.7 g) also presented with tumors at mammary glands 1-3, and smaller tumors at 6 and 7. Again, we examined an ROI in the upper body, but the imaging slice was higher positioned compared to the previous experiments, excluding the heart but including a portion of the mouse brain.

Anatomical ^{1}H MRI delineated the tumorous regions, revealing that the tumor in mammary gland 2 had progressed significantly, with a maximum diameter of 13 mm and notable T_2w+ areas, **Figure 4**. This facilitated comparison with previous observations from mouse B, **Figure 3**. In the HP ^{13}C MRI scan, consistent with previous results, robust pyruvate and lactate signals were detected in the tumors. Interestingly, the T_2w+ region again exhibited lower metabolic activity than the surrounding tumor tissue, **Figure 4**. Histological analysis indicated apoptosis onset in the latter region.

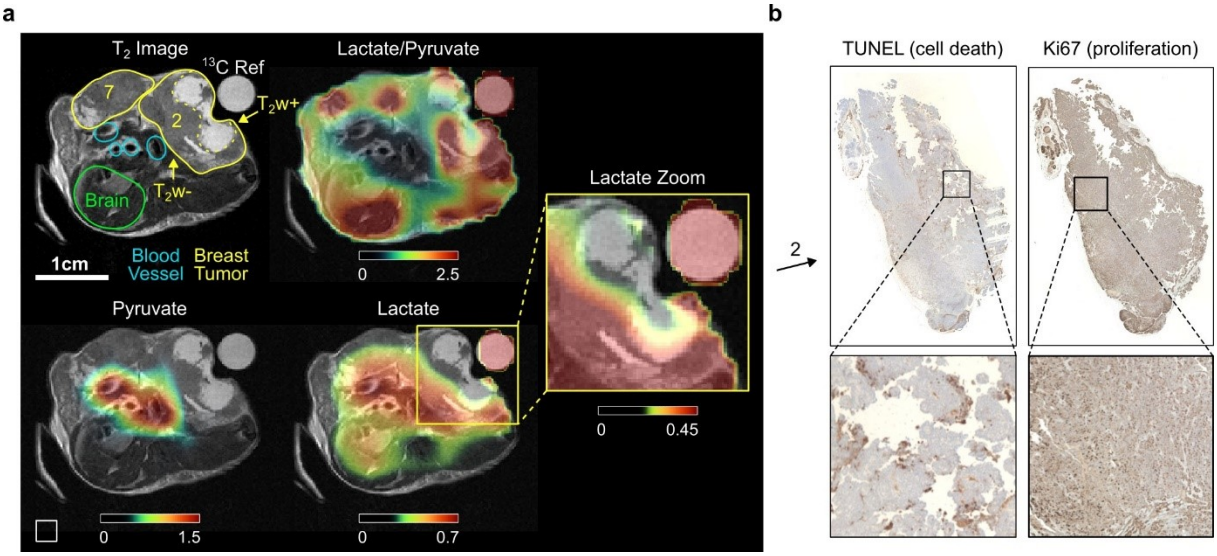

Figure 4. *In vivo* ^{1}H T_2w MRI and dynamic ^{13}C chemical shift imaging of PyMT mouse C after administering SABRE-hyperpolarized [1-^{13}C]-pyruvate-d_3 and histology of the imaged tumor. **a**, Axial anatomic ^{1}H MRI showing the tumors on mammary gland 2 and 7, brain, blood vessels, and a ^{13}C-lactate reference (left). The anatomic slice is superimposed with time-summated and interpolated ^{13}C-lactate/^{13}C-pyruvate (top right), ^{13}C-pyruvate (bottom left) and ^{13}C-lactate signal (bottom right). The heterogeneous breast tumor in mammary gland 2 divides into a hyper-intense (T_2w+) region with lower lactate and lactate-to-pyruvate signals and a hypo-intense (T_2w-) tumor region with higher signal. Note that low lactate signals can lead to high lactate-to-pyruvate ratios without significance if the pyruvate signal in the same voxel is negligible (no thresholding was applied to the ratio maps). The white box indicates the native CSI-FID resolution. **b**, Histology of the hypointense tumor region with TUNEL staining indicating ongoing apoptosis (left) and Ki67 staining indicating cell proliferation (right).

2.2.4. Summary of other mice and comparison

Three additional mice, D, E, and F, aged 12, 14, and 14 weeks respectively, were examined as detailed in the supplementary information (SI). They also exhibited localized tumor formations, consistent with observations from previous experiments, characterized by elevated ^{13}C signals and lactate metabolism in tumor areas compared to healthy tissue, e.g., **Figure S7**. As previously described, T_2w+ and necrotic regions showed meager ^{13}C signals, i.e. were metabolically less active, **Figure S6**. In some cases, the tumors exhibited poor pyruvate signals but strong lactate signals, indicating rapidly metabolized pyruvate (mice B and C, **Figure S6)**. The lactate-to-pyruvate ratios of different regions (T_2w+, T_2w-, and heart/blood vessel) from all six mice are compared in **Figure 5**. It appears that T_2w- tumor regions have a higher lactate-to-pyruvate ratio than T_2w+ tumor or heart/blood vessel, with a significant difference observed between T_2w- and heart/blood vessel tissues ($p < 0.001$). This trend was observed across all mice, as shown in **Figure S9**.

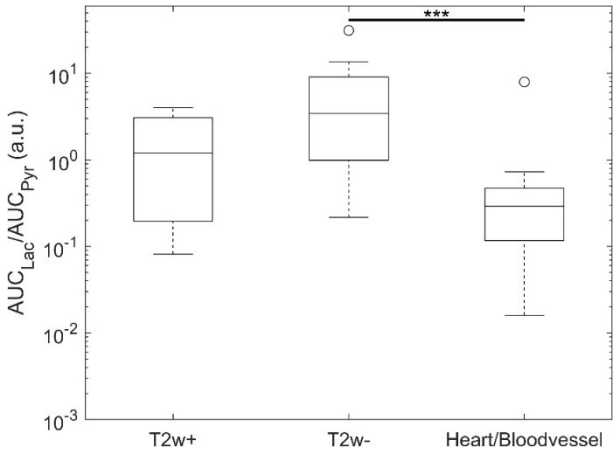

Figure 5. Box-and-whiskers plot depicting the lactate-to-pyruvate ratios across different regions in six mice: Hyperintense tumor (T_2w+), hypointense tumor (T_2w-), and heart resp. blood vessel (depending on the mouse). The significant difference between the T_2w- and heart/blood vessel is marked with *** ($p < 0.001$).

3. Significance and Conclusion

Breast cancer is one of the most prevalent tumor entities and has been studied extensively with dDNP-based HP MRI.[49,50] Also, the MMTV-PyMT mouse model has been studied before.[47] In this pilot study, we applied the less complex, low-cost, high-throughput SABRE approach for the first time to tumor imaging. Our methodology enables rapid preparation of HP pyruvate

without chemical modification for *in vivo* use within six minutes, utilizing a cost-effective (<10,000€), self-constructed setup.

In agreement with previous studies, we found elevated lactate formation as a manifestation of the Warburg effect in the tumors. Notably, we identified regional differences in pyruvate metabolism within the tumors in the ^{13}C MRI. These findings correlated with histological results, particularly with cell proliferation and apoptosis staining.

We utilized transgenic MMTV-PyMT breast cancer mice.[46–48] Tumor growth was fast, and substantial variations were observed between the six mice investigated. Via histology, we observed cell death onset within some tumors as the animals approached the ethical study endpoint regarding the primary tumor burden. Although this diversity in tumor stages complicates potential studies, the model is particularly intriguing because the mice hyper-activate key molecular pathways associated with breast cancer, such as PI3K signaling. The resulting stepwise tumor progression mirrors the tumor histopathology as well as the tumor stages of breast cancer patients. Therefore, the primary tumors of the MMTV-PyMT model present a range of metabolic tumor phenotypes that are likely to be encountered in clinical imaging studies. Notably, the clinical value of HP MRI has already been demonstrated in multiple clinical studies, including improved grading[9] and risk stratification for prostate cancer patients and characterization of tumor heterogeneity in glioblastoma.[51] Recent reports showed the capability of HP MRI to monitor treatment response to neoadjuvant chemotherapy in breast cancer patients within days.[11] Thus, the development of faster, cost-effective technologies is crucial for increasing the availability of this promising molecular imaging technique. However, translating SABRE to clinical applications will require significant effort. This includes increasing polarization levels, upscaling the polarizer, developing reliable automated purification procedures, obtaining cleaner solutions, and ensuring rapid quality assurance.

In conclusion, the present study demonstrates, for the first time, metabolic imaging of tumors with SLIC-SABRE hyperpolarized pyruvate. We have demonstrated that SABRE delivers the signal enhancement needed for detecting metabolic spatial differences in complex tumor tissue, possibly linked to different grades of proliferation and apoptosis. Note that with improved sequences, we also expect enhanced SNR and higher quality images.[52,53] This study demonstrates that SABRE has matured enough to allow cancer studies, significantly enhancing access to HP as a powerful molecular imaging tool and being a promising candidate for clinical translation.

Supporting Information

Please find additional experimental details, MRI, and mice data in the Supporting Information.

Acknowledgements

Research reported in this publication was supported by the German Federal Ministry of Education and Research (BMBF) in the funding program "Quantum Technologies – from Basic Research to Market" under the project "QuE-MRT" (contract number: 13N16448, 13N16450), the German Cancer Consortium (DKTK), the DKTK joint funding HYPERBOLIC, the Research Commission of the University Medical Center Freiburg, the Core Facility AMIR^{CF} (DFG-RIsources N° RI_00052, INST 39/1224-1), B.E.S.T. Fluidsysteme GmbH I Swagelok Stuttgart, and the German Research Foundation (DFG #SCHM 3694/1-1, #SCHM 3694/2-1, #SFB1479, #HO4604/4-1, #HO4604/5-1, #FOR5042), BMBF BlueHealthTech 03WIR6208A. EYC thanks NIBIB R21 EB033872.

Conflicts of Interest

SK and IS are with NVision Imaging Technologies GmbH. FS serves on the scientific advisory board of NVision Imaging Technologies GmbH. EYC holds a stake of ownership in XeUS Technologies Ltd. and serves on the scientific advisory board of Visma Life Sciences LLC. The other authors have no competing interests to declare.

References

[1] D. Zardavas, A. Irrthum, C. Swanton, M. Piccart, *Nat. Rev. Clin. Oncol.* **2015**, *12*, 381–394.

[2] S. P. Rowe, M. G. Pomper, *CA. Cancer J. Clin.* **2022**, *72*, 333–352.

[3] Z. J. Wang, M. A. Ohliger, P. E. Larson, J. W. Gordon, R. A. Bok, J. Slater, J. E. Villanueva-Meyer, C. P. Hess, J. Kurhanewicz, D. B. Vigneron, *Radiology* **2019**, *291*, 273.

[4] M. M. Chaumeil, J. A. Bankson, K. M. Brindle, S. Epstein, F. A. Gallagher, M. Grashei, C. Guglielmetti, J. D. Kaggie, K. R. Keshari, S. Knecht, C. Laustsen, A. B. Schmidt, D. Vigneron, Y.-F. Yen, F. Schilling, *Mol. Imaging Biol.* **2023**, DOI 10.1007/s11307-023-01888-5.

[5] J. H. Ardenkjær-Larsen, B. Fridlund, A. Gram, G. Hansson, L. Hansson, M. H. Lerche, R. Servin, M. Thaning, K. Golman, *Proc. Natl. Acad. Sci.* **2003**, *100*, 10158–10163.

[6] J. Kurhanewicz, D. B. Vigneron, J. H. Ardenkjaer-Larsen, J. A. Bankson, K. Brindle, C. H. Cunningham, F. A. Gallagher, K. R. Keshari, A. Kjaer, C. Laustsen, D. A. Mankoff,

M. E. Merritt, S. J. Nelson, J. M. Pauly, P. Lee, S. Ronen, D. J. Tyler, S. S. Rajan, D. M. Spielman, L. Wald, X. Zhang, C. R. Malloy, R. Rizi, *Neoplasia* **2019**, *21*, 1–16.

[7] F. Zaccagna, M. A. McLean, J. T. Grist, J. Kaggie, R. Mair, F. Riemer, R. Woitek, A. B. Gill, S. Deen, C. J. Daniels, S. Ursprung, R. F. Schulte, K. Allinson, A. Chhabra, M.-C. Laurent, M. Locke, A. Frary, S. Hilborne, I. Patterson, B. D. Carmo, R. Slough, I. Wilkinson, B. Basu, J. Wason, J. H. Gillard, T. Matys, C. Watts, S. J. Price, T. Santarius, M. J. Graves, S. Jefferies, K. M. Brindle, F. A. Gallagher, *Radiol. Imaging Cancer* **2022**, *4*, e210076.

[8] H.-Y. Chen, R. Aggarwal, R. A. Bok, M. A. Ohliger, Z. Zhu, P. Lee, J. W. Gordon, M. van Criekinge, L. Carvajal, J. B. Slater, P. E. Z. Larson, E. J. Small, J. Kurhanewicz, D. B. Vigneron, *Prostate Cancer Prostatic Dis.* **2020**, *23*, 269–276.

[9] R. Chowdhury, C. A. Mueller, L. Smith, F. Gong, M.-V. Papoutsaki, H. Rogers, T. Syer, S. Singh, G. Brembilla, A. Retter, M. Bullock, L. Caselton, M. Mathew, E. Dineen, T. Parry, J. Hennig, D. von Elverfeldt, A. B. Schmidt, J.-B. Hövener, M. Emberton, D. Atkinson, A. Bainbridge, D. G. Gadian, S. Punwani, *J. Magn. Reson. Imaging* **2023**, *57*, 1865–1875.

[10] N. Sushentsev, M. A. McLean, A. Y. Warren, A. J. V. Benjamin, C. Brodie, A. Frary, A. B. Gill, J. Jones, J. D. Kaggie, B. W. Lamb, M. J. Locke, J. L. Miller, I. G. Mills, A. N. Priest, F. J. L. Robb, N. Shah, R. F. Schulte, M. J. Graves, V. J. Gnanapragasam, K. M. Brindle, T. Barrett, F. A. Gallagher, *Nat. Commun.* **2022**, *13*, 466.

[11] R. Woitek, M. A. McLean, S. Ursprung, O. M. Rueda, R. Manzano Garcia, M. J. Locke, L. Beer, G. Baxter, L. Rundo, E. Provenzano, J. Kaggie, A. Patterson, A. Frary, J. Field-Rayner, V. Papalouka, J. Kane, A. J. V. Benjamin, A. B. Gill, A. N. Priest, D. Y. Lewis, R. Russell, A. Grimmer, B. White, B. Latimer-Bowman, I. Patterson, A. Schiller, B. Carmo, R. Slough, T. Lanz, J. Wason, R. F. Schulte, S.-F. Chin, M. J. Graves, F. J. Gilbert, J. E. Abraham, C. Caldas, K. M. Brindle, E. Sala, F. A. Gallagher, *Cancer Res.* **2021**, *81*, 6004–6017.

[12] R. Woitek, K. M. Brindle, *Diagnostics* **2023**, *13*, 2311.

[13] J. H. Ardenkjaer-Larsen, *J. Magn. Reson.* **2016**, *264*, 3–12.

[14] H. Park, Q. Wang, *Chem. Sci.* **2022**, *13*, 7378–7391.

[15] J. H. Ardenkjær-Larsen, S. Bowen, J. R. Petersen, O. Rybalko, M. S. Vinding, M. Ullisch, N. Chr. Nielsen, *Magn. Reson. Med.* **2019**, *81*, 2184–2194.

[16] A. Capozzi, T. Cheng, G. Boero, C. Roussel, A. Comment, *Nat. Commun.* **2017**, *8*, 15757.

[17] S. Jannin, A. Bornet, R. Melzi, G. Bodenhausen, *Chem. Phys. Lett.* **2012**, *549*, 99–102.

[18] Q. Stern, Q. Reynard-Feytis, S. J. Elliott, M. Ceillier, O. Cala, K. Ivanov, S. Jannin, *J. Am. Chem. Soc.* **2023**, *145*, 27576–27586.

[19] A. B. Schmidt, C. R. Bowers, K. Buckenmaier, E. Y. Chekmenev, H. de Maissin, J. Eills, F. Ellermann, S. Glöggler, J. W. Gordon, S. Knecht, I. V. Koptyug, J. Kuhn, A. N. Pravdivtsev, F. Reineri, T. Theis, K. Them, J.-B. Hövener, *Anal. Chem.* **2022**, *94*, 479–502.

[20] O. G. Salnikov, D. B. Burueva, I. V. Skovpin, I. V. Koptyug, *Mendeleev Commun.* **2023**, *33*, 583–596.

[21] C. R. Bowers, D. P. Weitekamp, *J. Am. Chem. Soc.* **1987**, *109*, 5541–5542.

[22] T. C. Eisenschmid, R. U. Kirss, P. P. Deutsch, S. I. Hommeltoft, R. Eisenberg, J. Bargon, R. G. Lawler, A. L. Balch, *J. Am. Chem. Soc.* **1987**, *109*, 8089–8091.

[23] F. Reineri, T. Boi, S. Aime, *Nat. Commun.* **2015**, *6*, 5858.

[24] E. Cavallari, C. Carrera, M. Sorge, G. Bonne, A. Muchir, S. Aime, F. Reineri, *Sci. Rep.* **2018**, *8*, 8366.

[25] T. Hune, S. Mamone, H. Schroeder, A. P. Jagtap, S. Sternkopf, G. Stevanato, S. Korchak, C. Fokken, C. A. Müller, A. B. Schmidt, D. Becker, S. Glöggler, *ChemPhysChem* **2023**, *24*, e202200615.

[26] L. Fries, T. Hune, S. Sternkopf, S. Mamone, K. L. Schneider, R. Schulz-Heddergott, D. Becker, S. Glöggler, *Chem. – Eur. J.* **n.d.**, *n/a*, e202400187.

[27] L. Nagel, M. Gierse, W. Gottwald, Z. Ahmadova, M. Grashei, P. Wolff, F. Josten, S. Karaali, C. A. Müller, S. Lucas, J. Scheuer, C. Müller, J. Blanchard, G. J. Topping, A. Wendlinger, N. Setzer, S. Sühnel, J. Handwerker, C. Vassiliou, F. H. A. van Heijster, S. Knecht, M. Keim, F. Schilling, I. Schwartz, *Adv. Sci.* **2023**, *10*, 2303441.

[28] R. W. Adams, J. A. Aguilar, K. D. Atkinson, M. J. Cowley, P. I. P. Elliott, S. B. Duckett, G. G. R. Green, I. G. Khazal, J. López-Serrano, D. C. Williamson, *Science* **2009**, *323*, 1708–1711.

[29] W. Iali, S. S. Roy, B. J. Tickner, F. Ahwal, A. J. Kennerley, S. B. Duckett, *Angew. Chem. Int. Ed.* **2019**, *58*, 10271–10275.

[30] M. J. Cowley, R. W. Adams, K. D. Atkinson, M. C. R. Cockett, S. B. Duckett, G. G. R. Green, J. A. B. Lohman, R. Kerssebaum, D. Kilgour, R. E. Mewis, *J. Am. Chem. Soc.* **2011**, *133*, 6134–6137.

[31] D. A. Barskiy, K. V. Kovtunov, I. V. Koptyug, P. He, K. A. Groome, Q. A. Best, F. Shi, B. M. Goodson, R. V. Shchepin, M. L. Truong, A. M. Coffey, K. W. Waddell, E. Y. Chekmenev, *ChemPhysChem* **2014**, *15*, 4100–4107.

[32] J.-B. Hövener, N. Schwaderlapp, T. Lickert, S. B. Duckett, R. E. Mewis, L. A. R. Highton, S. M. Kenny, G. G. R. Green, D. Leibfritz, J. G. Korvink, J. Hennig, D. von Elverfeldt, *Nat. Commun.* **2013**, *4*, 2946.

[33] T. Theis, M. L. Truong, A. M. Coffey, R. V. Shchepin, K. W. Waddell, F. Shi, B. M. Goodson, W. S. Warren, E. Y. Chekmenev, *J. Am. Chem. Soc.* **2015**, *137*, 1404–1407.

[34] V. V. Zhivonitko, I. V. Skovpin, I. V. Koptyug, *Chem. Commun.* **2015**, *51*, 2506–2509.

[35] J.-B. Hövener, A. N. Pravdivtsev, B. Kidd, C. R. Bowers, S. Glöggler, K. V. Kovtunov, M. Plaumann, R. Katz-Brull, K. Buckenmaier, A. Jerschow, F. Reineri, T. Theis, R. V. Shchepin, S. Wagner, P. Bhattacharya, N. M. Zacharias, E. Y. Chekmenev, *Angew. Chem. Int. Ed.* **2018**, *57*, 11140–11162.

[36] B. Chapman, B. Joalland, C. Meersman, J. Ettedgui, R. E. Swenson, M. C. Krishna, P. Nikolaou, K. V. Kovtunov, O. G. Salnikov, I. V. Koptyug, M. E. Gemeinhardt, B. M. Goodson, R. V. Shchepin, E. Y. Chekmenev, *Anal. Chem.* **2021**, *93*, 8476–8483.

[37] I. Adelabu, P. TomHon, M. S. H. Kabir, S. Nantogma, M. Abdulmojeed, I. Mandzhieva, J. Ettedgui, R. E. Swenson, M. C. Krishna, T. Theis, B. M. Goodson, E. Y. Chekmenev, *ChemPhysChem* **2022**, *23*, e202100839.

[38] "Catalyst-Free Aqueous Hyperpolarized [1-13C]Pyruvate Obtained by Re-Dissolution Signal Amplification by Reversible Exchange | ACS Sensors," can be found under https://pubs.acs.org/doi/full/10.1021/acssensors.2c01715, **n.d.**

[39] K. MacCulloch, A. Browning, D. O. Guarin Bedoya, S. J. McBride, M. B. Abdulmojeed, C. Dedesma, B. M. Goodson, M. S. Rosen, E. Y. Chekmenev, Y.-F. Yen, P. TomHon, T. Theis, *J. Magn. Reson. Open* **2023**, *16–17*, 100129.

[40] S. J. DeVience, R. L. Walsworth, M. S. Rosen, *Phys. Rev. Lett.* **2013**, *111*, 173002.

[41] T. Theis, M. Truong, A. M. Coffey, E. Y. Chekmenev, W. S. Warren, *J. Magn. Reson.* **2014**, *248*, 23–26.

[42] A. B. Schmidt, J. Eills, L. Dagys, M. Gierse, M. Keim, S. Lucas, M. Bock, I. Schwartz, M. Zaitsev, E. Y. Chekmenev, S. Knecht, *J. Phys. Chem. Lett.* **2023**, *14*, 5305–5309.

[43] A. N. Pravdivtsev, K. Buckenmaier, N. Kempf, G. Stevanato, K. Scheffler, J. Engelmann, M. Plaumann, R. Koerber, J.-B. Hövener, T. Theis, *J. Phys. Chem. C* **2023**, *127*, 6744–6753.

[44] H. de Maissin, P. R. Groß, O. Mohiuddin, M. Weigt, L. Nagel, M. Herzog, Z. Wang, R. Willing, W. Reichardt, M. Pichotka, L. Heß, T. Reinheckel, H. J. Jessen, R. Zeiser, M. Bock, D. von Elverfeldt, M. Zaitsev, S. Korchak, S. Glöggler, J.-B. Hövener, E. Y. Chekmenev, F. Schilling, S. Knecht, A. B. Schmidt, *Angew. Chem. Int. Ed.* **2023**, *62*, e202306654.

[45] A. M. Funk, X. Wen, T. Hever, N. R. Maptue, C. Khemtong, A. D. Sherry, C. R. Malloy, *J. Magn. Reson.* **2019**, *301*, 102–108.

[46] S. Ketterer, J. Mitschke, A. Ketscher, M. Schlimpert, W. Reichardt, N. Baeuerle, M. E. Hess, P. Metzger, M. Boerries, C. Peters, B. Kammerer, T. Brummer, F. Steinberg, T. Reinheckel, *Nat. Commun.* **2020**, *11*, 5133.

[47] S. Asghar Butt, L. V. Søgaard, J. H. Ardenkjaer-Larsen, M. H. Lauritzen, L. H. Engelholm, O. B. Paulson, O. Mirza, S. Holck, P. Magnusson, P. Åkeson, *Magn. Reson. Med.* **2015**, *73*, 51–58.

[48] S. Attalla, T. Taifour, T. Bui, W. Muller, *Oncogene* **2021**, *40*, 475–491.

[49] R. Woitek, K. M. Brindle, *Diagnostics* **2023**, *13*, 2311.

[50] O. Arponen, P. Wodtke, F. A. Gallagher, R. Woitek, *Eur. J. Radiol.* **2023**, *167*, 111058.

[51] S. J. Nelson, J. Kurhanewicz, D. B. Vigneron, P. E. Z. Larson, A. L. Harzstark, M. Ferrone, M. van Criekinge, J. W. Chang, R. Bok, I. Park, G. Reed, L. Carvajal, E. J. Small, P. Munster, V. K. Weinberg, J. H. Ardenkjaer-Larsen, A. P. Chen, R. E. Hurd, L.-I. Odegardstuen, F. J. Robb, J. Tropp, J. A. Murray, *Sci. Transl. Med.* **2013**, *5*, 198ra108-198ra108.

[52] P. E. Z. Larson, J. M. L. Bernard, J. A. Bankson, N. Bøgh, R. A. Bok, A. P. Chen, C. H. Cunningham, J. W. Gordon, J.-B. Hövener, C. Laustsen, D. Mayer, M. A. McLean, F. Schilling, J. B. Slater, J.-L. Vanderheyden, C. von Morze, D. B. Vigneron, D. Xu, *Magn. Reson. Med.* **2024**, *91*, 2204–2228.

[53] J. W. Gordon, H.-Y. Chen, N. Dwork, S. Tang, P. E. Z. Larson, *J. Magn. Reson. Imaging* **2021**, *53*, 686–702.